Towards integration of GNSS and GB-SAR measurements: Exemplary monitoring of a rock fall at the Yangtze River in China

Aiham HASSAN, Germany, Jinjun XU, China, Li ZHANG, Germany, Guanlan LIU, China, Annette SCHMITT, Germany, Cheng XING, China, Yaming XU, China, Chenhao OUYANG, China, Volker SCHWIEGER, Germany

Key words: Engineering survey, GB-SAR, GNSS, Monitoring, Deformation measurement, Rock fall

SUMMARY

Monitoring of artificial or natural objects is essential to reduce the risk of hazards. In order to get more accurate and reliable monitoring results, a huge research effort was made in the last decades. The reliability of monitoring can be improved by integration of at least two independent measuring techniques and in this paper, a first approach to integrate GNSS and GB-SAR measurements, while monitoring a rock fall at the Yangtze River near the Three Gorges Dam in China is presented. The site is unstable due to natural conditions such as the active geological structure, variation of water level, and human interventions like coal mining.

Nowadays the ground-based Synthetic Aperture radar (GB-SAR) is gaining more importance in the field of monitoring, because of its high temporal and spatial resolution and its high accuracy in detection of movements and displacements in the line of sight (LOS) direction. In contrast GNSS has a low spatial resolution (pointwise measurements). The advantage of the GNSS is the ability to detect 3D-displacements precisely.

Using both techniques, a first trial was made; the aim of this investigation is the detection of possible problems that could occur during the measurement or data processing and to judge the measuring and integration concept proposed here. In this trial, two GNSS-reference stations and the GB-SAR instrument (IBIS-L) were installed in a stable area; about 700 m away from the movement area. Another two GNSS-rover stations were installed in the rock fall area. In order to detect the positions of the GNSS-rover stations in the GB-SAR data and thus to compare the GNSS-results with those obtained by GB-SAR, two RADAR corner cubes were installed near the GNSS-rover stations. Furthermore, the meteorological data are measured in order to investigate the correlation between atmospheric parameter variations and GB-SAR observations.

During the measurements campaign the results of GNSS show no significant displacement, in contrast the results of GB-SAR show a LOS-displacement of several mm, which are traceable to atmospheric changes. After the atmospheric correction using ground control points (GCPs) and transformation to the GNSS-coordinate system the displacement time series obtained by GB-SAR are comparable with those measured by GNSS. The atmospheric correction issue

should be further investigated in the future. Furthermore, the corner cubes could not be realized unambiguously in the data of the GB-SAR. Using bigger corner cubes and improving their orientation could be helpful in the next measurement campaign.

Towards integration of GNSS and GB-SAR measurements: Exemplary monitoring of a rock fall at the Yangtze River in China

Aiham HASSAN, Germany, Jinjun XU, China, Li ZHANG, Germany, Guanlan LIU, China, Annette SCHMITT, Germany, Cheng XING, China, Yaming XU, China, Chenhao OUYANG, China, Volker SCHWIEGER, Germany

1. INTRODUCTION AND ROCK FALL DISCRIPTION

Landslides and rock falls (L&R) are major natural hazards. They cause a great loss of lives and property worldwide every year. Monitoring surveys are widely used in order to identify possible hazards at an early time and thus to avoid or reduce the risk of those hazards. Monitoring survey is the survey to determine movements and deformations of technical and natural objects. It covers all required measures: planning, realization, evaluation and documentation (translated from DIN 18710-4, 2010). Based on the monitoring results and in case of existing danger the monitoring area can be either evacuated or stabilized through constructive measures such as slide-resistant pile and anchorage in case of L&R.

In this paper, the case study approach will focus on the Lianziya, a rock fall located on the south-west side of the Yangtze River, 27 km upper Three-Gorges Dam (China), opposite to the Xintan-landslide which occurred on June 12, 1985 (Figure 1).

Figure 1: The geographical location of Lianziya (Google earth）

The site is unstable due to natural conditions such as the active geological structure, variation of water level, and human interventions like coal mining. About 60 cracks have been formed due to the long term directional displacement. This constitutes a direct threat to the shipping on Yangtze River and the surrounding towns. A continuously geological survey and research of Lianziya started from the late 1960s. Plenty of geological exploring, scientific experiments,

internal and external deformation monitoring data have been obtained. Lianziya is divided into three areas according to geological structures, topography and the Characteristics of movement (see Figure 2, (Wang, 1999)).

These three areas are cut by several cracks whose information is shown in Table 1.

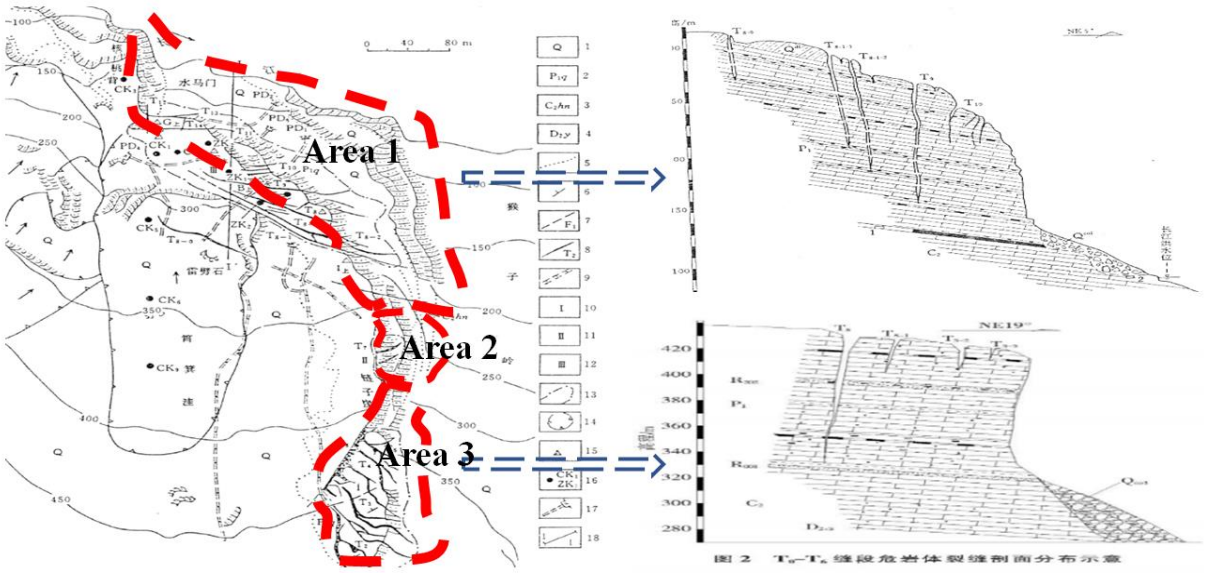

Figure 2: Divided areas and geological structure of Lianziya (Wang, 1999)

Table 1: Geometric information of Lianziya (Wang, 1999)

area	Top elevation [m]	Rock trend	Long [m]	Wide [m]	High [m]	Volume [m^3]
area 1	500-410	South-North	210	50	90-100	$90x10^4$
area 2	390-370	South-North	50	8	54-60	$2x10^4$
area 3	330-180	East-West	320	80	90-100	$230x10^4$

In order to ensure safety of the shipping on Yangtze River and Three-Gorges Dam, different treatments are applied to these three areas depending on the deformation states, topography and the extend of risk. Constructive measures were applied in area 1 (close to the Yangtze River) from May 1993 to September 1999, after that the area tended to be stable (Yi, 2006). A monitoring method of intersection using total stations is employed in the area 2 and area 3. The recently geological exploring and external deformation monitoring indicates that the deformation in area 3 is still active, caused by the water-level change of reservoir, and the adverse geological structure. The average annual horizontal displacement is about 1.0~4.2 mm in direction north-east (to the valley). The average annual vertical displacement is about 0.3~2.9 mm (Tu, 2011).

In this paper, a measuring procedure for integration of GNSS and the Ground-based Synthetic Aperture Radar (GB-SAR) measurements while monitoring the area 3 at the Lianziya rock fall is presented. GNSS is a real-time monitoring technique, which can detect 3D-displacements precisely but in a low spatial resolution (pointwise). In contrast, GB-SAR can measure in a high spatial resolution and a high accuracy displacements in the line of sight (LOS). However, these displacements in LOS will be practical significance only when transformed to a 3D coordinate system. Using both techniques, a more accurate and reliable deformation distribution can be obtained and offers scientific basis for subsequent stability analysis.

2. BASICS

2.1 Monitoring

Nowadays monitoring tasks become more important, because the safety and operational capability has to be ensured and risks have to be minimized. Due to that reason, objects, which imperil the human beings and infrastructure, have to be monitored. In the last decades several monitoring approaches with different kinds of sensors and different monitoring intervals are developed (Heunecke et al, 2013).

For every object, which should be monitored, an individual monitoring concept has to be developed. Highly dynamic object like bridges or towers should be monitored steadily, compared to slow moving rock falls, which could be monitored in a periodical cycle (Heunecke et al, 2013). The choice of the instruments used for the monitoring depends also on the dynamic of the object. For dynamic objects GNSS, total station, GB-SAR and inclination sensors could be used. Slow moving objects could be monitored additionally with Laser scanners or photogrammetry. The selection of the instrument depends also on the size and kind of the monitored objects. One question is, if pointwise monitoring is sufficient or if an area wise is required.

In the context of this project an area wise monitoring is requested. Therefore the pointwise GNSS is combined with the areal GB-SAR. Due to the fact that the rock fall moves very slowly, the measurements are done periodically and area wise.

2.2 Principle and advantage of GB-SAR

GB-SAR is a remote sensing technique developed for monitoring of natural and artificial objects. The ground based technique has been proposed and developed based on the same air- and space borne technique by the Joint Research Center (JRC) of the European Commission in the late 90´s (Rudolf et al., 1999) and became commercially available at the beginning of the last decade as the instrument IBIS-L (Image by Interferometric Survey) has been developed by the Italian company Ingegneria dei Sistemi S.p.A. (IDS) in collaboration with the Department of Electronics and Telecommunication of the Florence University (Rödelsperger, 2011).

IBIS-L uses the technique of Stepped Frequency Continuous Wave (SF-CW) (Paulose, 1994) to achieve a range resolution of 0.5 m and the SAR technique to achieve a cross range resolution of 4.4 mrad. SAR technique uses multiple acquisitions of a given scene from separate positions to refine the cross-range resolution. The multiple acquisitions are achieved in the case of IBIS-L by moving the radar along a two meter rail. After establishing the resolution of the result image, the movements of individual pixels (and therefore parts of observed object) can be computed by the differential interferometry method. This method uses differences in phase values about pixels from two (or more) acquisitions to determine their relative movement.

Comparing to other monitoring techniques i.e. GNSS, extensometer etc. GB-SAR allows monitoring the area of interest contactless, independent from daylight and almost regardless of climatic conditions. The result is a high accurate continuous map of movements for the whole illuminated area. Furthermore the radar can be wirelessly connected to remote processing and supervising station and the movements can be detected in real time.

In the last years several studies discussed the reliability and accuracy of GB-SAR and approved its potential in monitoring of landslide movements (Leva et al., 2003; Herrera et al., 2009; Luzi et al., 2010), glacier (Luzi et al., 2007), snow avalanche (Martinez-Vazquez & Fortuny-Guasch, 2008) and generation of a Digital Elevation Model (Rödelsperger et al., 2010). The above mentioned studies and applications are just some examples without claim of completeness.

2.3 GNSS

Accuracies in the mm range can be achieved by applying geodetic GNSS receivers using carrier phase measurement in relative mode. Beside tachymeters, only GNSS receivers can measure the 3-dimensional positions automatically and continuously. So, GNSS receivers have already been used in the monitoring very early, for example, a GPS monitoring system has been developed at the Graz University of Technology (Hartinger, 2001). Multi-GNSS (Wanninger, 2008) and PPP technic (precise point positioning, Heßelbarth, 2011, Choy et al., 2017) and Low-Cost GNSS (Zhang et al., 2012) are recent trends of GNSS.

3. TEST SCENARIO

Measurements were carried out from 18:30 o'clock, September 9, 2017 to 20:00 o'clock, September 11, 2017. The whole experiment took about 50 hours. The GB-SAR was fixed on a platform which is built on a stable area and aims at the center of deformation area with a clinometer to level the track. The platform is about 700 m away from the Lianziya rock fall. The maximum measurement distance is set to 1000 m and the elevation angle 10º. The SAR-image acquisition frequency was six minutes; at last 540 images were obtained. Figure 3 shows the installation of IBIS-L and the monitoring scene.

Figure 3: Installation of IBIS (left) and monitoring scene (right)

Two GNSS-reference stations were also installed near the GB-SAR instrument in a stable area and another two GNSS-rover stations were installed in the rock fall area. In order to detect the positions of the GNSS-rover stations in the GB-SAR data and thus to compare the GNSS-results with those obtained by GB-SAR, two RADAR corner cubes were installed near the GNSS-rover stations, the GNSS stations are equipped with dual-frequency geodetic GNSS receivers Trimble NetR9 and Trimble Zephyr 3 geodetic GNSS Antennas (see Figure 5), which can receive the signals from GPS, GLONASS and Beidou. An overview of the GNSS stations is shown in Figure 4. Base station 1 is near the GB-SAR station, base station 2 is as a backup for the base station 1. Both stations are under open-sky condition and about 130 m apart from each other. The distance between the two rover stations are about 55 m, the obstructions in both stations are in north direction. The distance between the base stations and rover stations are about 700 m, the height differences are about 200 m. The sampling rate of GNSS receivers is set to 15 seconds.

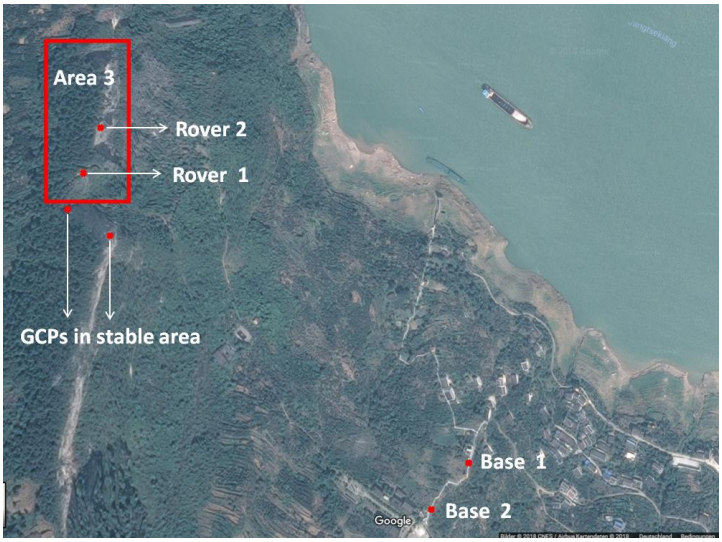

Figure 4: Overview of GNSS stations and GCPs in stable area

a) Base station 1 b) Base station 2 c) Rover station 1 d) Rover station 2

Figure 5: GNSS Stations

Furthermore, the meteorological data (temperature, humidity and pressure) on the GB-SAR station and in the monitoring area were collected every 10 minutes in order to investigate the influence of atmospheric disturbances on the observations obtained by the GB-SAR.

4. DATA PROCESSING AND ANALYSIS

To avoid the data gapes occurred during the measurements, just the data obtained from September, 10 at 9:00 o'clock to September, 11 at 12:00 o'clock were been considered during the processing.

4.1 GB-SAR Data processing

The reflectivity of the illuminated area can be represented through the Thermal Signal to Noise Ratio (TSNR) image. TSNR is the ratio between the power of the received signal and the thermal noise power of the instrument in dB and can be computed for each pixel in each epoch. As shown in TSNR image (Figure 6 left) the monitoring rock body (area 3) has a high reflection to the SAR signal, this complicates the detection of the corner cubes in the SAR-image.

Based on the interferometry phase between two or more epochs i.e. images, the LOS displacement for the whole illuminated area between two or more epochs can be determined and represented in an interference displacement-gram (Figure 6 right). The TSNR image and the two images used for the interference displacement-gram in Figure 6 are selected from the 307 images randomly.

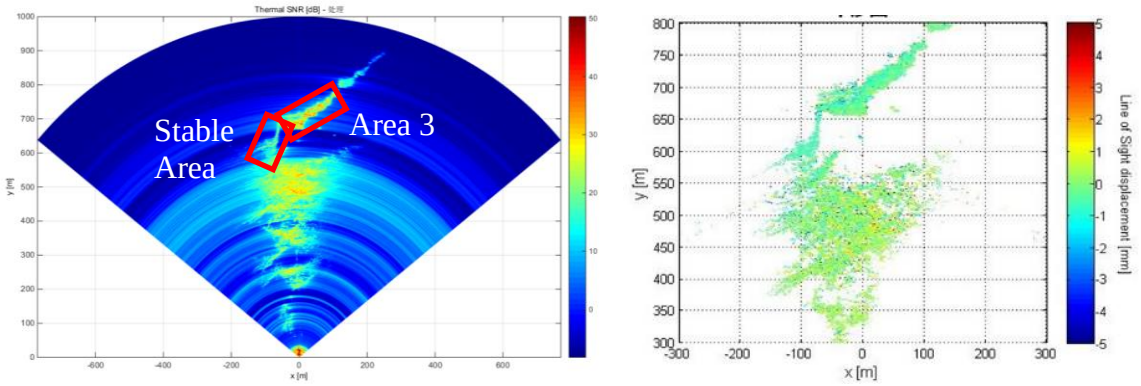

Figure 6: SAR Image; TSNR image (left) and displacement gram (right)

The interferometry phase φ_w can be expressed as

$$\varphi_w = \varphi_{disp} + \varphi_{atm} + \varphi_{noise} - 2N\pi , \tag{1}$$

where φ_{disp} is the phase component related to the actual displacement, φ_{atm} is the phase component due to atmospheric effect during image acquisition, φ_{noise} is phase component by all kinds of noise and N is the integer phase ambiguity. As the phase shift detected by the instrument is only in the range $\varphi_{disp}[-\pi, \pi]$, the integer value N should be determined when a displacement lager than $\frac{\lambda}{4}$ occurs. This operation is named phase unwrapping, where λ is the wavelength of the emitted signal.

The propagation of the radar wave through the atmosphere is influenced by the variation of refractive index of the atmosphere n. For a single f frequency radar wave, phase of echo from a target with distance r can be determined as

$$\varphi = \frac{4\pi f}{c} \int n(r,t)dr , \tag{2}$$

with c is the velocity of light in vacuum, n being the refractive index which changes in time and location. For a fixed target, the refractive index n only depends on time t. If two echoes from the motionless target are acquired at time t_1 and t_2, a phase difference can be expressed as

$$\varphi_{atm} = \varphi(t_2) - \varphi(t_1) = \frac{4\pi f}{c}(n(t_2) - n(t_1)). \tag{3}$$

If the atmospheric condition changes between time t_1 and t_2, the refractive index $n(t_2) \neq n(t_1)$, then $\varphi_{atm} \neq 0$.

After atmospheric disturbance elimination and phase unwrapping, the relationship between displacement Δ and interferometry phase φ can be expressed as

$$\Delta = -\frac{\lambda}{4\pi}\varphi_{disp} \quad . \tag{4}$$

4.1.1 Importance of atmospheric correction for GB-SAR Data

Ignoring the phase shift caused by atmospheric disturbances (φ_{atm}) during the measurements the displacement time series were computed for six pixels selected in area 3 (Figure 7 left). These time series (Figure 7 right) show a LOS-displacement up to 15 mm within a measurement period of 27 hours. Taking into account an expected annual deformation of not more than 5 mm in area 3, the whole area can be considered as stable during the measurement period and the apparent displacements could be just due to the atmospheric variation during the measurements.

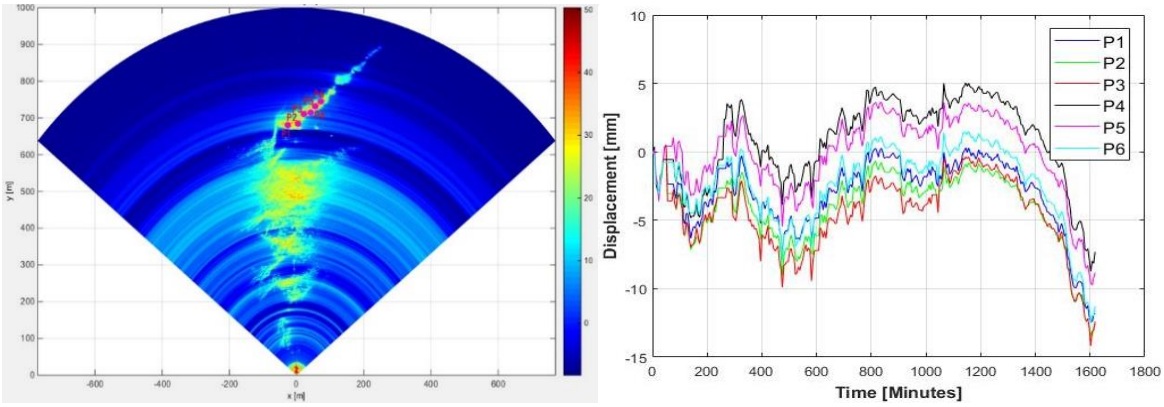

Figure 7: Selected pixels in area 3 (left) and LOS-displacement time series for some pixels without atmospheric correction (right)

To approve this result, the dependency represented through the cross correlation coefficients between these displacement time series and the measured time series of the atmospheric parameters (humidity, temperature and air pressure) variations are shown in Table 2. This table approved the strong dependency between both time series, the atmospheric phase and thus the measured displacement is very sensitive to the variation of humidity (77 ~ 83%) and temperature (-64 ~ -82%) and less sensitive to the variation of air pressure with one exception in the time series of P4.

Table 2: Cross correlation between displacement time series in the selected pixels and atmospheric parameter variations

Pixel	P1	P2	P3	P4	P5	P6	Mean
Humidity Δh	0.83	0.83	0.77	0.77	0.80	0.81	0.80
Temperature ΔT	-0.73	-0.72	-0.64	-0.82	-0.74	-0.70	-0.73
Air pressure ΔP	0.03	0.03	0.06	0.33	0.16	-0.08	0.09

4.1.2 Determination of atmospheric effect by ground control points (GCPs)

The atmospheric phase component φ_{atm} can be eliminated through three different ways:

(1) Determination of the atmospheric effects by meteorological observations (temperature, humidity and pressure) in the monitoring area between sensor and targets（further details in Liebe, 1981)

(2) Determination of the atmospheric effects by ground control points (GCPs). These GCPs should be either stable during the measurements or their true displacement have to be determined through further measurements i.e. GNSS or Total station. Furthermore GCP must be of good quality pixels (good TSNR and coherence) and located near the area of interest.

(3) Spatial interpolation or filtering (e. g. Meyer et al., 2005)

The second method is applied in this paper once with two stable GCPs selected near area 3 (Figure 8 Up-left and Figure 4) and once with two GCPs selected within the area 3 (Figure 8 Up-right), which displacement was measured by means of GNSS (Rover 1 and Rover 2).

Assuming a uniform atmosphere (i.e. constant atmospheric parameters), the atmospheric phase component depends only on the distance r between sensor and target:

$$\varphi_{\text{atm}} = \frac{4\pi}{\lambda} a.r + \varepsilon \ , \tag{5}$$

where ε is the measurement noise.

For the stable GCPs the displacement phase is $\varphi_{disp} = 0$ and the atmospheric phase can be determined directly using formula (1). For the GCPs within area 3 the displacement is known (from GNSS measurements) and φ_{disp} can be determined using formula (4). So the atmospheric phase for the GCPs can be determined using formula (1). In both cases the correction coefficient a in formula (5) can be calculated in each time step and then φ_{atm} can be determined for each pixel in area 3 and eliminated. For modelling the atmospheric variations along the path higher order models could be also used:

$$\varphi_{\text{atm}} = \frac{4\pi}{\lambda} \sum_{i=0}^{n} a_i . r^i + \varepsilon \, . \tag{6}$$

The corrected time series for the same pixels shown in Figure 7 are shown in Figure 8 down left for correction using stable GPCs and downright using GPCs in area 3.

Both methods lead to a significant improvement of the derived displacement time series. The time series in case of atmospheric correction using stable GCPs (Figure 8 down left) show a decreasing trend for the pixels P3, P4, P5 and P6 and a displacement up to -3.5 mm with some local jumps up to -3.5 mm; the time series of pixels P1 and P2, which are located near the selected GCPs, are more stable and show no significant trend. The correlation coefficients with atmospheric variations (Table 3) is significantly decreased comparing to those with the non-corrected displacement time series (Table 2); the mean correlation with humidity variations is decreased from 80% to 53% and with temperature variations from -73% to -50% (for the absolute values). Even that the correlation with the air pressure increased for some pixels significantly, the different signs for those correlations for different pixels conclude that those correlations are not systematic.

The time series in the another case (GCPs in area 3) are more stable and show no clear trend with a displacement up to 0,5 mm and less local jumps up to 2 mm, which can be caused by the measurement noise. The efficiency of the atmospheric correction can be represented through the correlation coefficients with the atmospheric parameter time series (Table 4). These are decreased in case of humidity to a mean value of 18%, in case of temperature to -20% and are in case of air pressure not systematic for the same reason mentioned above. The results of this correction method seem to be, in this study case, the most promising results and will be therefor used for further processing.

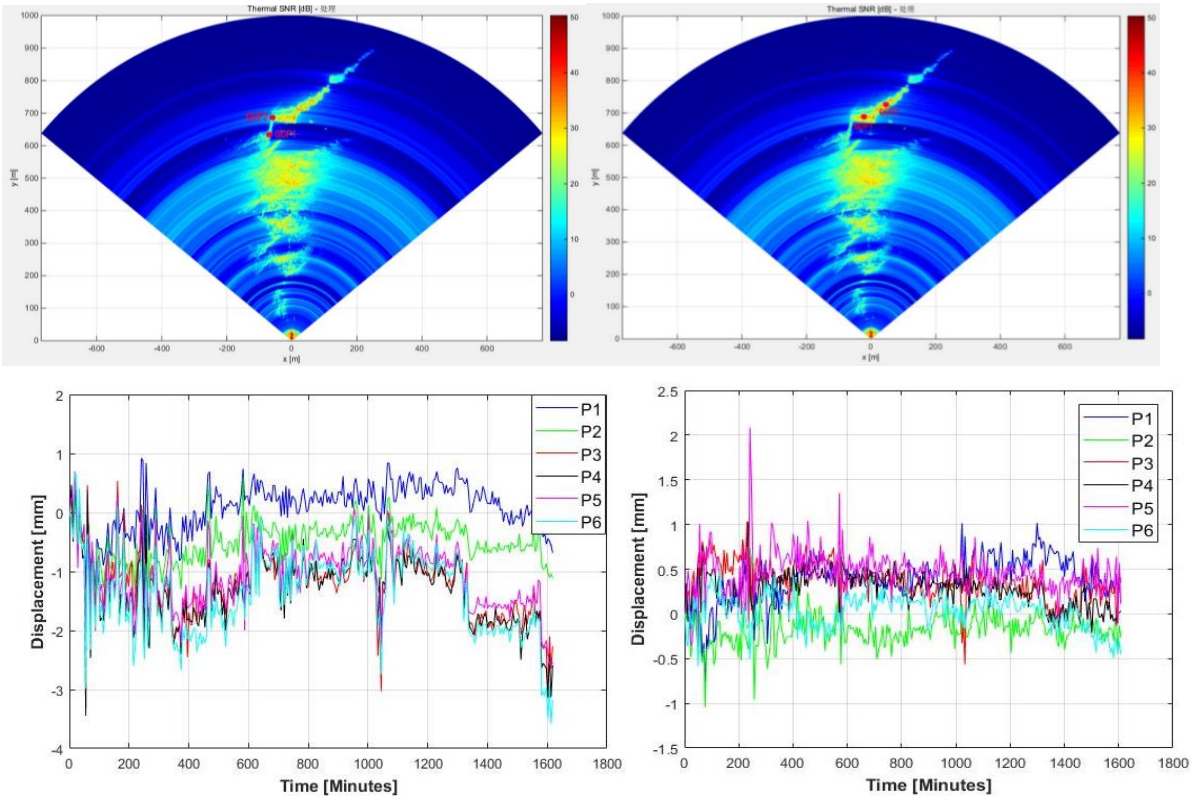

Figure 8: Up: Selected GCPs in a stable area (left) and in area 3 (right). Down: LOS-displacement time series for some pixels with an atmospheric correction using GCPs in a stable area (left) and in area 3 (right)

Table 3: Cross correlation between displacement time series in the selected pixels corrected using GCPs in a stable area and atmospheric parameter variations

Pixel	P1	P2	P3	P4	P5	P6	Mean
Humidity Δh	0.39	0.41	0.52	0.62	0.61	0.67	0.53
Temperature ΔT	-0.54	-0.47	-0.37	-0.52	-0.52	-0.57	-0.50
Air pressure ΔP	0.46	0.26	-0.20	-0.11	-0.03	0.01	0.07

Table 4: Cross correlation between displacement time series in the selected pixels corrected using GCPs in area 3 and atmospheric parameters variations

Pixel	P1	P2	P3	P4	P5	P6	Mean
Humidity Δh	0.11	0.08	-0.02	0.35	0.06	0.52	0.18
Temperature ΔT	-0.34	-0.15	0.13	-0.33	-0.10	-0.43	-0.20
Air pressure ΔP	0.43	0.08	-0.53	-0.37	-0.13	-0.12	-0.11

4.2 GNSS

The GNSS baselines are processed by the software Grafnav (Grafnav, 2018), the elevation angle is set to 10°. As an example the original residuals of baseline base station 1 to rover station 1 are shown in Figure 9. The outliers can be identified with the 3σ method (DIN 18709-5, 2010) and linear interpolated.

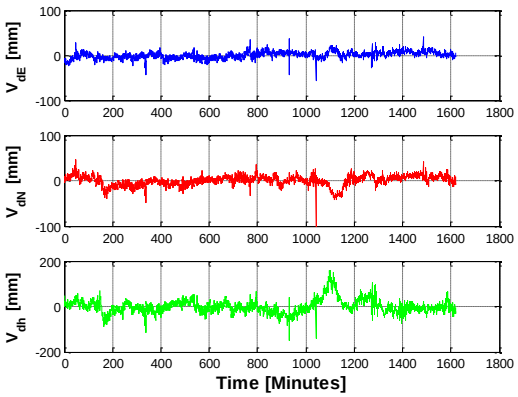

Figure 9: Original residuals baseline Base 1- Rover 1

The base station 1 worked very well and has no gaps. It is near to the GB-SAR station, so only the baseline from base station 1 will be analysed below. The percentage of the outliers and the standard deviation of the baselines are calculated and can be regarded as reliability and accuracy of the GNSS measurements respectively (Zhang et al. 2012). The results are shown in Table 5. The standard deviation in height is about 2 to 3 factors higher than that in horizontal components. Although the baselines are quite short, only about 700 m, the height difference of about 200 m is quite large. In consequence it is possible that the tropospheric error is not completely eliminated by double differencing.

Since on rover station 2 there are more obstructions than on rover station 1 (compare Figure 5c and 5d), the standard deviations of the baseline Base 1 - Rover 1 are better than that of baseline Base 1 - Rover 2. Besides, baseline Base 1 - Rover 1 has less outliers than baseline Base1 - Rover 2. Furthermore the obstructions on both rover stations are in north direction, so that is the reason that for both baselines the standard deviation in North is larger than that in East.

Table 5: Percentage of outliers and standard deviations of the original baselines

Baseline	Percentage of outlier [%]	Standard deviation in East [mm]	Standard deviation in North [mm]	Standard deviation in Height [mm]
Base 1-Rover 1	1.5	6.9	9.8	24.8
Base 1-Rover 2	1.8	13.4	19.0	32.3

Since the selected pixel P1 from the GB-SAR is located in the area where the rover station 1 was set up, just the displacement time series between these two points can be compared. So for this reason only the base line Base 1 - Rover 1 will be investigated in the following. The correlation between the baselines and the atmospheric variations are also analysed. The sample rate of the GNSS measurements and meteorological data are 15 seconds and 10 minutes respectively, the mean value of GNSS data are calculated for every 10 minutes. The combined mean values of the meteorological data (humidity, temperature and pressure) on base station 1 and rover station are calculated, and then the cross correlations are calculated. The correlation coefficients at the time shift of zero between the baseline residuals and humidity, temperature and pressure are 0.03, 0.06 and 0.384 respectively. The quite high correlation between the baseline residuals and the pressure is probably because of the tropospheric influence caused by the height difference between Base 1and Rover 1.

5. COMPARE OF GB-SAR AND GNSS TIME SERIES

5.1 Coordinate system transformation from GB-SAR to GNSS

The LOS-displacement is a projection and thus a part of the real displacement (Figure 10). In contrast the GNSS displacement vector represents the real displacement vector. In order to compare the 3D-displacement obtained by GNSS-measurements with the LOS-displacements obtained by GB-SAR-measurements, the LOS-displacement should be projected on the coordinate axes of the 3D-GNSS displacements. For this purpose, the coordinate of the centre of GB-SAR's track has been measured by GNSS. Two corner cubes (Monitoring 1 and Monitoring 2) were installed in area 3 near rover 1 and rover 2 respectively. Monitoring 1, which is identical with selected pixel P1, has been measured by GNSS during GB-SAR data collecting. So, the LOS-directions from the centre of GB-SAR to Monitoring 1 and Monitoring 2 in the coordinate system of GNSS are determined and the LOS-displacement can be transformed into 3D-GNSS as following:

Suppose that the coordinates of the centre of GB-SAR are $N_{SAR}, E_{SAR}, H_{SAR}$ in the coordinate system of GNSS, and for the monitoring point are N_{Mo}, E_{Mo}, H_{Mo}, the direction vector of the LOS-displacement is

$$\alpha_{LOS} = \left(\frac{N_{SAR} - N_{Mo}}{S}, \frac{E_{SAR} - E_{Mo}}{S}, \frac{H_{SAR} - H_{Mo}}{S}\right), \tag{7}$$

where S is the slope distance from GB-SAR to the monitoring point.

The direction vector of the real-displacement represented through the GNSS displacement vector is

$$\alpha_{GNSS} = \left(\frac{\Delta N_{GNSS}}{\Delta_{GNSS}}, \frac{\Delta E_{GNSS}}{\Delta_{GNSS}}, \frac{\Delta H_{SAR}}{\Delta_{GNSS}}\right), \tag{8}$$

where $\Delta_{GNSS} = \sqrt{\Delta N_{GNSS}^2 + \Delta E_{GNSS}^2 + \Delta H_{GNSS}^2}$ is the absolute GNSS-displacement.

The angle β between both direction vectors is then:

$$\cos(\beta) = \alpha_{LOS} . \alpha_{GNSS} \tag{9}$$

and the projected SAR displacement Δ_{SAR} can be computed from the measured-LOS displacement:

$$\Delta_{SAR} = \frac{\Delta_{LOS}}{\cos(\beta)} . \tag{10}$$

The relationship between the SAR displacement Δ_{SAR} and the coordinate system of GNSS can be expressed as

$$\begin{aligned} \Delta N &= \Delta_{SAR}.\cos(Z).\cos(\mathrm{A}) \\ \Delta E &= \Delta_{SAR}.\cos(Z).\sin(\mathrm{A}) \\ \Delta H &= \Delta_{SAR}.\sin(Z) \end{aligned} \tag{11}$$

where A is the azimuth and Z the zenith. They can be calculated by equation (8).

$$\begin{aligned} A &= \cos^{-1}((N_{Mo} - N_{SAR}) / S_h) \\ Z &= tg^{-1}((H_{Mo} - H_{SAR}) / S_h) \end{aligned} \tag{12}$$

with $S_{\mathrm{h}} = \sqrt{(N_{Mo} - N_{SAR})^2 + (E_{Mo} - E_{SAR})^2}$

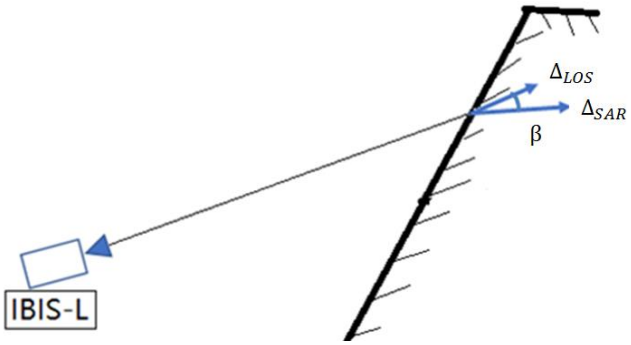

Figure 10: LOS-movement (Δ_{LOS}) and real movement measured by SAR (Δ_{SAR})

The 3-D displacement time series obtained by GB-SAR for P1 are shown in Figure 11.

5.2 Results and discussion

The displacements measured by GB-SAR for pixel P1 are transformed in the East, North and Height components (Figure 11), the horizontal components (North and East) are smaller, have less jumps and less standard deviation (Table 6) comparing to the height component, similar result was also obtained by GNSS (see 4.2). Considering the standard deviations of GNSS and GB-SAR there is no significant difference between the GNSS and GB-SAR results. Because the sampling rate of GB-SAR and GNSS data are different, the GB-SAR data are interpolated,

then the cross correlations between GB-SAR and GNSS measurements are calculated, the mean value of the correlation coefficients at the time shift zero is only 0.096. This indicates to the stochastic nature of both time series.

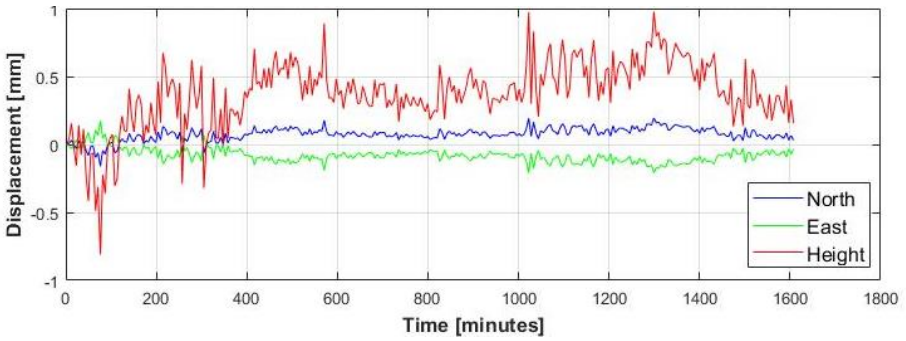

Figure 11: Transformed 3D-displacement time series obtaind by GB-SAR

Table 6: Standard deviation of transformed 3D-displacement time series obtaind by GB-SAR

Component	East	North	Height
Standard deviation [mm]	0.05	0.05	0.24

6. CONCLUSION AND OUTLOOK

For a long-term field observation with GB-SAR, atmospheric corrections have to be considered. An accurate and reliable way is the correction model based on GCPs. It is recommended to use more and well distributed GCPs around or in monitoring area. In this paper the none-corrected GB-SAR data show displacements up to 15 mm and a strong dependency on the variations of the atmospheric parameters. This dependency represented through the correlation coefficient is very high with humidity (80%) and temperature (-72%) and less with air pressure (9%). Using stable GCPs to correct this atmospheric influence decreases the obtained displacements to a maximum value of 3.5 mm and the correlations with the variations of humidity, temperature and air pressure to 53%, -50% and 7% respectively. The best correction results are achieved in this paper through using GCPs within the monitoring area. The displacement of theses GCPs is determined using GNSS measurements. In this case no significant displacements are obtained from GB-SAR data and the correlation coefficients with the variations of humidity, temperature and air pressure decreases to 18%, -20% and 11% respectively. These GCPs can also be applied as identical points for coordinate system transformation between GNSS and GB-SAR in order to compare the results of both techniques. The comparison between both techniques shows no significant differences; the displacements obtained by GNSS and by GB-SAR are not significant.

Because of the high reflectivity of the rock body in area 3 and the bad orientation of the corner cubes, the positions of these cubes could not be determined unambiguously in GB-SAR images, it is recommended to optimize the orientation of these cubes and maybe use larger cubes in the next epoch.

In the next epoch, not only the geodetic GNSS system but also the low-cost GNSS system, e.g. from U-blox, will be set up in the test field. The influence of multipath effect should be analysed and reduced significantly. The tropospheric influence will be further investigated in the future. Furthermore terrestrial laser scanning will be used in order to improve the reliability of the monitoring results.

ACKNOWLEDGEMENT

The investigations published in this article are granted by the DAAD (German Academic Exchange Service) project Nr. 5731774 and CSC (China Scholarship Council) within PPP (Project Based Personnel Exchange Program). Therefore the authors cordially thank the funding agencies.

REFERENCES

Choy, S.; Harima, K.; Rizos, C.; Kogure, S. (2017): An investigation into the performance of real-time GPS+GLONASS Precise Point Positioning (PPP) in New Zealand In: Journal of Applied Geodesy, 11, 185 – 195.

DIN 18709-5 (2010): Begriffe, Kurzzeichen und Formelzeichen, in der Geodäsie - Teil 5: Auswertung kontinuierlicher Messreihen. Beuth Verlag, Berlin.

DIN 18710-4 (2010): Ingenieurvermessung - Teil 4: Überwachung. Beuth Verlag, Berlin.

Grafnav (2018):https://www.novatel.com/products/software/grafnav/. Last access:07.02.2018.

Herrera, G.; Fernández-Merodo, J. A.; Mulas, J.; Pastor, M.; Luzi, G.; Monserrat, O. (2009): A landslide forecasting model using ground based SAR data: The Portalet case study. Engineering Geology, 105(3), 220-230.

Heunecke, O.; Kuhlmann, H.; Welsch, W.; Eichhorn, A.; Neuner, H. (2013): Handbuch der Ingenieurgeodäsie – Auswertung geodätischer Überwachungsmessung. 2nd, newly overworked and extented Edition. Wichmann Verlag, Berlin.

Heßelbarth, A. (2011): Statische und kinematische GNSS-Auswertung mittels Precise Point Positioning (PPP). Dissertationen at TU Dresden, Deutsche Geodätische Kommission, München, Reihe C, Nr. 667.

Hartinger, H. (2001): Development of a Continuous Deformation Monitoring System using GPS. Shaker Verlag, Aachen 2001.

Leva, D.; Nico, G.; Tarchi, D.; Fortuny-Guasch, J.; Sieber, A. J. (2003): Temporal analysis of a landslide by means of a ground-based SAR interferometer. IEEE Transactions on Geoscience and Remote Sensing, 41(4), 745-752.

Liebe，H. J. (1981): Modeling attenuation and phase of radio waves in air at frequencies below 100 GHz. Radio Science. Volume 16, No.6, 1183-1200.

Luzi, G.; Pieraccini, M.; Mecatti, D.; Noferini, L.; Macaluso, G.; Tamburini, A.; Atzeni, C. (2007): Monitoring of an alpine glacier by means of ground-based SAR interferometry. IEEE Geoscience and Remote Sensing Letters, 4(3), 495-499.

Luzi, G.; Monserrat, O.; Crosetto, M.; Copons, R.; Altimir, J. (2010): Ground-based SAR interferometry applied to landslide monitoring in mountainous areas. In Mountain Risks conference: Bringing Science to Society, Firenze (IT), 24-26.

Martinez-Vazquez, A. & Fortuny-Guasch, J. (2008): A GB-SAR processor for snow avalanche identification. IEEE Transactions on Geoscience and Remote Sensing, 46(11), 3948-3956.

Meyer, F.; Kampes, B.; Bamler, R.; Fischer, J. (2006): Methods for atmospheric correction in InSAR data. In Fringe (2005) Workshop (Vol. 610).

Paulose, A. (1994): High radar range resolution with the step frequency waveform. Naval Postgraduate school Monterey CA.

Rödelsperger, S.; Becker, M.; Gerstenecker, C.; Läufer, G.; Schilling, K.; Steineck, D. (2010): Digital elevation model with the ground-based SAR IBIS-L as basis for volcanic deformation monitoring. Journal of Geodynamics, 49(3), 241-246.

Rödelsperger, S. (2011): Real-time processing of ground based synthetic aperture radar (GB-SAR) measurements (No. 33). Technische Universität Darmstadt, Fachbereich Bauingenieurwesen und Geodäsie.

Rudolf, H.; Leva, D.; Tarchi, D.; Sieber, A. J. (1999): A mobile and versatile SAR system. In: Geoscience and Remote Sensing Symposium, 1999. IGARSS'99 Proceedings. IEEE 1999 International (Vol. 1, 592-594).

Tu, P.F.; Wu, X.W. (2011): Study on Deformation and Failure Mechanism of Lianzi Cliff Dangerous Rock Body in Three Georges Reservoir Area. Subgrade Engineering, No.1/154, 38-40+44 (in Chinese language).

Wang, S.Q. (1999): Monitoring and Forecast of Landslides in The Three Georges of Yangtze River. Geological publishing house (in Chinese language).

Wanninger, L. (2008): The Future is Now - GPS + GLONASS + SBAS = GNSS. GPS World, Volume 19, Issue 7, 42-48.

Yi, W. (2006): Deformation Monitoring of T8-T12 Fracture Sections at Lianzi Cliff of Three Gorges. Disaster And Control Engineering. No.2/61, 28-32 (in Chinese language).

Zhang, L.; Stange, M.; Schwieger, V. (2012): Automatic Low-Cost GPS Monitoring System Using WLAN Communication. FIG Working Week, Rom.

BIOGRAPHICAL NOTES

M.Sc. **Aiham Hassan**

2001– 2006 Studies of Civil Engineering at Tishreen University in Latakia, Syria (Degree: B.Sc.)
2007– 2010 Research Associate at Institute of Topographie, Tishreen University in Latakia, Syria
2011 – 2014 Studies of Geodesy and Geoinformation at Technical University of Darmstadt (Degree: M.Sc.)
Since 2014 Research Associate at Institute of Engineering Geodesy, University of Stuttgart

Prof. Dr. **Jinjun Xu**

1981–1986 Studies and B. SC. (Tongji University)
1988 M.Sc. (Wuhan Technical University of Surveying and Mapping)
1990 Lecturer (Wuhan Technical University of Surveying and Mapping)
2002 Ph.D. Geodesy (University of Wuhan)
2007 Professor Geodesy and Geomatics (University of Wuhan)

Dr.-Ing. **Li Zhang**

2002 – 2003 Studies of Geodesy in China (University of Wuhan)
2004 – 2009 Studies of Geodesy and Geoinformation in Germany (University of Stuttgart)
2009 Research Associate at Institute of Engineering Geodesy, University of Stuttgart
2015 Vice Chair of Administration of FIG Commission 5 "Positioning and Measurement"
2016 Dr.-Ing. Geodesy (University of Stuttgart)

Dr. **Guanlan Liu**

200–2005 Studies and B. SC. Geodesy and Geomatics (University of Wuhan)
2007 M.Sc. Geodesy and Geomatics (University of Wuhan)
2013 Ph. D. Geodesy and Geomatics (University of Wuhan)
2015 Visiting Scholar at Leibniz University of Hannover

M.Sc. **Annette Schmitt**

2006 – 2010 Studies of Geodesy and Geomatics at University of Applied Sciences Karlsruhe (Degree: B.Sc.)
2010 – 2013 Studies of Geodesy and Geoinformatics at Karlsruhe Institute of Technology (Degree: M.Sc.)
Since 2013 Research Associate at Institute of Engineering Geodesy, University Stuttgart

Dr. **Cheng Xing**

2001–2005 Studies and B. SC., Geodesy and Geomatics (University of Wuhan)
2006–2011 Ph. D. Geodesy and Geomatics (University of Wuhan)
2009–2010 Joint training (University of New South Wales)
2011 Lecturer (University of Wuhan)

Prof. Dr. **Yaming Xu**

1983–1987 Studies and B. SC. (Wuhan Technical University of Surveying and Mapping)
1990 M.Sc. and Lecturer (Wuhan Technical University of Surveying and Mapping)
1997 Vice Professor Geodesy (Wuhan Technical University of Surveying and Mapping)
2002 Ph.D. Geodesy (University of Wuhan)
2004 Professor Geodesy and Geomatics (University of Wuhan)

Mr. **Chenhao Ouyang**

2013–2017 Studies and Bachelor Geodesy (University of Wuhan)
2017 Studies of Geodesy of University of Wuhan, Master Program

Prof. Dr.-Ing. habil. **Volker Schwieger**

1983 – 1989 Studies of Geodesy in Hannover
1989 Dipl.-Ing. Geodesy (University of Hannover)
1998 Dr.-Ing. Geodesy (University of Hannover)
2004 Habilitation (University of Stuttgart)
2010 Professor and Head of Institute of Engineering Geodesy, University of Stuttgart
2015 Chair of FIG Commission 5 "Positioning and Measurement"
2016 Dean of Faculty 6: Aerospace Engineering and Geodesy, University of Stuttgart

CONTACTS

M.Sc. Aiham Hassan
Institute of Engineering Geodesy, University of Stuttgart
Geschwister-Scholl-Str. 24D
Stuttgart
Germany
Tel. +49-711-685-84042
Fax + 49-711-685-84044
Email: Aiham.hassan@ingeo.uni-stuttgart.de
Web site: www.uni-stuttgart.de/ingeo

Prof. Dr. Jinjun Xu
Wuhan University
School of Geodesy and Geomatics
Institute of Surveying Engineering
129 Luoyu Road
Wuhan, 430079
P. R. CHINA
Tel. + 86/27-687-58563
Fax + 86/27-68778371
Email: jjxu@sgg.whu.edu.cn
Web site: http://ise.sgg.whu.edu.cn